Hydrodynamics of frontal striking in aquatic snakes: drag, added mass, and the possible consequences for prey capture success

Marion Segall, Anthony Herrel, Ramiro Godoy-Diana

Hydrodynamics of frontal striking in aquatic snakes: drag, added mass, and the possible consequences for prey capture success.

Marion Segall*[1,2,3], Anthony Herrel[1,4] and Ramiro Godoy-Diana[2].

1. UMR CNRS/MNHN 7179, « Mécanismes adaptatifs et Evolution », 55 Rue Buffon, 75005, Paris, France.
2. Laboratoire de Physique et Mécanique des Milieux Hétérogènes (PMMH), UMR CNRS 7636 ; ESPCI Paris, PSL Research University, Sorbonne Université, Université Paris Diderot, 75005 Paris, France.
3. Department of Herpetology, American Museum of Natural History, Central Park West at 79th Street, New York, NY 10024.
4. Evolutionary Morphology of Vertebrates, Ghent University, K.L. Ledeganckstraat 35, B-9000 Ghent, Belgium.

Corresponding author: Marion Segall, marion.segall@live.fr

Running title: Hydrodynamics of snake prey capture

Summary statement: The present work explores the functional implications of head shape in a group of aquatic predators using a fluid mechanics approach.

Abstract

Transient locomotion under water is highly constrained by drag and added mass, yet some aquatic snakes catch their prey using a fast forward acceleration, with the mouth opened. These aquatic snakes show a convergence of their head shape in comparison with closely related species that do not forage under water. As both drag and added mass are related to some extent to the shape of the moving object, we explored how shape impacts the hydrodynamic forces applied to the head of a snake during a prey capture event. We compared two 3D-printed heads representing typical shapes of aquatically-foraging and non-aquatically-foraging snakes, and frontal strike kinematics based on *in vivo* observations. By using direct force measurements, we calculated the drag and added mass coefficient of the two models. Our results show that both drag and added mass are reduced in aquatic snakes. The drag coefficient of the aquatic model is 0.24, which is almost two times smaller than the non-aquatic model. The added mass coefficient of the aquatic model is 0.15 versus 0.24 for the non-aquatic model, showing that the convergence of head shape in aquatically foraging snakes is associated with a hydrodynamic advantage during frontal striking. The vorticity field measurements with particle image velocimetry show that a less intense recirculation bubble behind the jaw of the aquatic model, compared to the non-aquatic model, might be the basis of this advantage.

Key words: snakes, fluid mechanics, forces, morphology, transient motion

Introduction

Aquatic animals have to overcome the strong viscous and inertial constraints associated with underwater motion [1]. Physically, these constraints are related to the kinematics of movement and the morphology of an animal (i.e. the shape of the object that is facing the flow). For most aquatic vertebrates, viscous effects are confined to a thin boundary layer surrounding the body, which couples the motion of the animal with that of the surrounding fluid and gives rise to the skin friction that penalizes aquatic locomotion. In addition, fluid inertia causes the boundary layer to separate from the animal's body, creating the recirculation zones associated to pressure drag [2]. The specifics of the flow separation determine the relative importance of pressure to skin friction drag [3,4]. Pressure drag and skin friction constitute together the steady drag, which depends on the velocity of the animal. During transient maneuvers, such as predatory strikes or predator escapes, an additional constraint is involved: the acceleration reaction[2,5]. This force that opposes the motion is related to the acceleration the animal imposes on the surrounding fluid while accelerating its own body mass. The mass of fluid that is accelerated along with the mass of the animal is called the added mass and it depends on the acceleration [5,6]. Both drag and added mass depend, to some extent, on the size and shape of the body [5]. As transient maneuvers are involved in survival-related behavior (foraging and predator avoidance), one can expect that the morphology of aquatic animals has evolved to reduce both drag and added mass.

However, the morphology of an animal is also constrained by evolutionary history, functional trade-offs, and developmental programs, thus restricting the range of possible morphological adaptations. Environmental and biological constraints act simultaneously on an organism and may all impact their evolution, sometimes leading to convergent phenotypes [7–10]. These shape convergences occur when constraints are strong, and solutions limited. These designs are particularly interesting from an engineering point of view as the shape results from a long-term selection often over millions of years and thus can provide insights to create new, more efficient designs. There is a continuum between streamlined objects and bluff bodies, but in most cases, hydrodynamic studies focus on rather simple geometries (e.g. sphere, cylinder, plates…; see [2]). We here propose to assess how more subtle shape changes may affect both drag and added mass and the possible functional implications of such changes.

Capturing elusive prey under water usually involves fast, accelerated motions of the predator (or part of it) towards the prey [11] which inevitably involves both drag and acceleration reaction. Among aquatic tetrapod predators, both snakes[12–17] and turtles use a fast forward motion of the head. The latter have, however, developed suction feeding to overcome the strong physical constraints [18–20]. Snakes cannot perform suction because of the reduction of their hyoid apparatus [15,21], yet convergence in head shape in aquatic snakes has been demonstrated several times [15,22–25]. As hydrodynamics and shape are intricately related, it is possible that the physical constraints have driven the convergent evolution of the head of snakes toward a more efficient shape (i.e. reducing drag and added mass) [1,26,27]. In a previous study [25], we compared the head shape of 62 species of snakes that capture prey under water (from sea snakes over homalopsids to North American watersnakes) versus 21 phylogenetically closely related species that do not forage under water. Using 3D geometric morphometrics in a phylogenetic framework, we demonstrated morphological convergence in the shape of the head of aquatically foraging snakes and we characterized the shapes that are specific to both groups of snakes (i.e. the aquatic and the non-aquatic foragers). We hypothesized that the head shape of aquatically foraging snakes provides them with a hydrodynamic advantage during the strike and is more efficient. The hydrodynamic constraints involved during a strike are the pressure drag – skin friction being negligible in the regimes of interest here [28] – and the added mass. Both of these constraints are related to a certain extent to the shape of the object that is moving through a fluid [5,6]. Thus, if our hypothesis is correct, the shape corresponding to the aquatic snake should induce less drag and a reduced added mass compared to the non-aquatic snake.

Another constraint related to the capture of prey under water is the mechano-sensitivity of aquatic prey like fish. The lateral line system of fish is composed of mechanoreceptors that can detect very small pressure variations with an estimated threshold of 0.1 to 1 mPa at 1 mm [29,30]. This system triggers a reflex escape response in the prey once a pressure threshold has been reached. Previous studies have suggested that a snake moving underwater generates a bow wave that might be able to trigger the reflex response of the prey [15,28]. We predicted that aquatic snakes should be stealthier than non-aquatic snakes during the strike, such that the detection of the predator by the prey would be delayed.

We used direct force measurements using two 3D printed models of snake heads derived from our previous work based on the comparison of 83 species of snakes [25] (i.e. more than 400 snake specimens). As these models result from a 3D geometric morphometric analysis, the models are scaled to the same size, allowing us to specifically test for the impact of shape on hydrodynamic constraints. Our experimental setup mimics a 'sit-and-wait' frontal strike under water, meaning that the model remains motionless before the strike and is then suddenly accelerated. The frontal strike is the strategy used by snakes to catch non-aquatic prey, and even though another aquatic prey capture strategy exists (lateral strike[17]), many aquatic snake species use fast forward strikes[12–16]. We decided to focus on this strategy as it has been associated with some piscivorous specialists and as it is allegedly the most hydrodynamically constrained [27]. We measured the force applied to the head during the strike to calculate the added mass and drag, which determine the hydrodynamic efficiency of a shape. In addition, another sensor was placed at the end of the strike track at the level of the model to assess the distance at which a prey is likely to detect the presence of the snake during capture. Particle Image Velocimetry (PIV) was used to visualize the flow field around the head during a strike. We also characterized the evolution of the vortex intensity during a strike for each shape, as it is closely related to the hydrodynamic forces generated by a moving object [31–33].

Material & Methods

3D models

We assessed the impact of shape on hydrodynamics by comparing two models of head shape of snakes that we termed "aquatic" and "non-aquatic" (Fig. 1a.). These shapes result from a 3D geometric morphometric study showing that the head shape of aquatic snake species has converged [25]. We measured the hydrodynamic forces that are exerted on each of the head shapes during a mimicked capture event. The shapes are the result from a geometric morphometrics analysis, meaning they went through a process (i.e. Generalized Procrustes Analysis) that scales the models to the same size (i.e. centroid size of 1.0) and removes differences in position by translating and rotating the models (see [34]). Thus, the only difference between the models is their shape. As snakes catch their prey with the mouth opened, we divided the two models in a homologous way by cutting the head in three parts (the top of the head, the jaw, and the rear of the head) following the same landmarks on each model. Then, we used Blender™ to rotate the

jaw and the top of the head to reach an angle of 70° based on previously published data on frontal strikes in snakes [14–16] (Supplementary Material 1). The two models were then 3D printed using a Stratasys Fortus 250 MC 3D printer with ABS P430 as a material, no surface treatment was applied to the models after printing (Fig. 1a.).

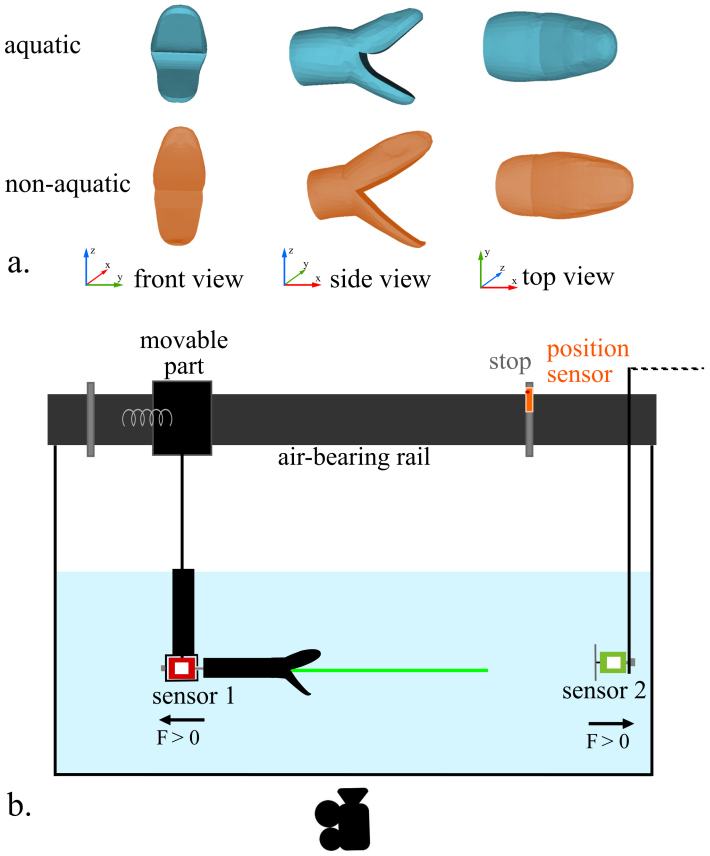

Figure 1: a. 3D models of the head shape of aquatic (first line) and non-aquatic snakes (second line) in front, side and top view (see also Supplementary Material 1). b. Experimental setup used to mimic the frontal attack of a snake towards a prey (see also Supplementary Material 2). The snake model is directly linked to the force sensor 1 which is itself vertically attached to the mobile part of the air-bearing rail. The force sensor 2 is placed at the end of the track. It is recording the pressure variation thanks to a round plate attached to the sensor (vertical grey line). The directions of the positive forces of each sensor is indicated (F > 0). The position sensor is placed at the end of the track, on the rail. The horizontal green line represents the laser sheet used for the PIV. The model is turned to obtain three different views of the flow pattern around the head (see Supplementary Material 3).

Experimental setup

Snakes capture their prey by using an explosive strike toward it, meaning that they generate a high acceleration once the prey is within reach[35]. Many species of aquatically foraging snakes use a fast forward strike. To mimic this behavior, we projected our models using two springs (Fig. 1b.). Our system is composed of two parts: a rail and a mobile part (Fig. 1b.). The rail insured a strict forward motion of the mobile part. The movable part is composed of the cart that can move along the rail with negligible friction thanks to the air-injection system and two springs, on the left and right part of the cart that allow to generate a transient motion in our system. A copper tube of diameter 1.5 cm is attached to the cart and plunges into the water. We designed a NACA profile to cover the part of the tube that is immersed into the water and we add a space to screw the force sensor 1 (FUTEK LSB210+/-2 Lb; Fig. 1b.). The model is horizontally attached to the force sensor using an aluminum rod of 5 mm diameter. Thus, the model is pushed by the force sensor.

For each strike, the two springs on each side of the cart are compressed against a vertical platform attached to the rail. The cart is held in the compressed position for a few seconds, so we got a resting value for the sensors. Then, the cart is released thus generating a transient motion of the cart and the model. The strike stopped when the cart hit the foam stop at the end of the track. We used different compressions of the springs to generate a range of speeds and accelerations. Approximately 60 strikes (i.e. spring compressions) were performed for each model. To obtain the kinematics of each strike, we recorded the position of the movable part using a position sensor (optoNCDT1420, Micro-Epsilon) (Fig. 1b.). The kinematics of the strike, namely the velocity $U_{(t)}$ and the acceleration $a_{(t)}$ (Fig. 2), are computed from the output of the position sensor using Eq (1) and Eq (2)

$$U_{(t)} = \frac{x_{(t+dt)} - x_{(t)}}{dt}; Eq\ (1),$$

$$a_{(t)} = \frac{U_{(t+dt)} - U_{(t)}}{dt};\ Eq\ (2),$$

where $x_{(t)}$ is the filtered position of the model recorded by the sensor at instant t, $U_{(t)}$ is the instantaneous velocity and $a_{(t)}$is the instantaneous acceleration. $x_{(t)}$ and $U_{(t)}$ were filtered using the moving average filter with a moving average of 50.

In addition, we wanted to assess what a prey would sense in terms of pressure, so we placed another, more sensitive, force sensor (FUTEK LSB210 100 g) at the end of the path in line with the moving model, to which we attached a round plastic piece of 7 cm in diameter that allowed us to record the pressure changes (sensor 2, Fig. 1b., Fig. 2b.). Thus, we were able to detect pressure variations of approximately 0.01 Pa which is in the range of the hearing and the startle threshold of some fish (i.e. between 0.01 Pa and 0.56 Pa) [36,37]. The force and position sensors were synchronized, and data were recorded at 1 kHz (Fig. 2).

Drag coefficient and added mass

Our primary goal was to characterize the hydrodynamic profile of our two head models by using the output of the force sensor 1. The forces involved in our experiment are the steady drag (F_d), the acceleration reaction (F_a) and the solid inertia of our model [6] (Fig. 3). The forces recorded can be expressed as follow [2]:

$$F = F_d + F_a + ma;\ Eq\ (3),$$

$$F = \frac{1}{2}\rho {U_{(t)}}^2 C_d S + C_a \rho V a + ma;\ Eq\ (4),$$

where ρ is the density of water, $U_{(t)}$ the velocity at the instant of interest and S the projected frontal surface area of the model, C_d is the drag coefficient of the model, m is the mass of the model, C_a is the added mass coefficient of the model, V is the volume of the model, a is the acceleration.

First, we calculated the drag coefficient of each model by solving $Eq\ (4)$ when $a = 0$ and $U = U_{max}$. When the system is not accelerated, the force measured by the sensor 1 is pure steady drag; $F = F_d$. The force reaches a plateau, but the signal is oscillating so we took the average value of this plateau as a measure of the steady drag force F_d (Fig. 2a.). Then, we calculated the drag coefficient (C_d):

$$C_d = \frac{2F_d}{\rho {U_{max}}^2 S} \; ; Eq\ (5)$$

The term $2F_d/\rho S$ was plotted against U^2 and the linear regression coefficient corresponds to the drag coefficient of the models (Fig. 4.). This representation allows to visualize the experimental data and to check the consistency of the measurement. The Reynolds number range of our experiments is 10^4 - 7.10^4 which is consistent with previous observations[1].

To calculate the added mass coefficient of each model, C_a, we chose the instant t when $a = a_{max}$ as it also corresponds to the peak of the force measured by the sensor:

$$C_a = \frac{F_{(t)} - F_{d(t)} - ma_{(t)}}{\rho V a_{(t)}}; \; Eq\ (4),$$

$$C_a = \frac{F_{(t)} - \frac{1}{2}\rho {U_{(t)}}^2 C_d S - ma_{(t)}}{\rho V a_{(t)}}; \; Eq\ (5)$$

where $F_{d(t)}$ is the "instantaneous drag". For simplification, we named the numerator of *Eq (7)*: F_M, such as: $F_M = F_{(t)} - \frac{1}{2}\rho {U_{(t)}}^2 C_d S - ma_{(t)}$. To obtain the added mass coefficient, we plotted $F_M/\rho V$, against the acceleration a. The linear regression coefficient corresponds to the added mass coefficient of the models (Fig. 4.). See table 1 for the features of each 3D printed model.

Model	***m (mass; g)***	***S (frontal surface; m²)***	***V (volume; m³)***
Aquatic	0.047	0.0012894	0.000073398
Non-aquatic	0.041	0.0014715	0.000057877

Table 1: Characteristics of each model.

Detection distance

To compare the effect of the head shape on the detection by a prey, we used the output of the second force sensor (sensor 2, Fig. 1b.). To estimate the position at which the prey could detect the predator, we defined the detection distance as the position at which the force detected

by sensor 2 deviates from the resting value by more than one standard deviation (Fig 2b., Fig. 5.).

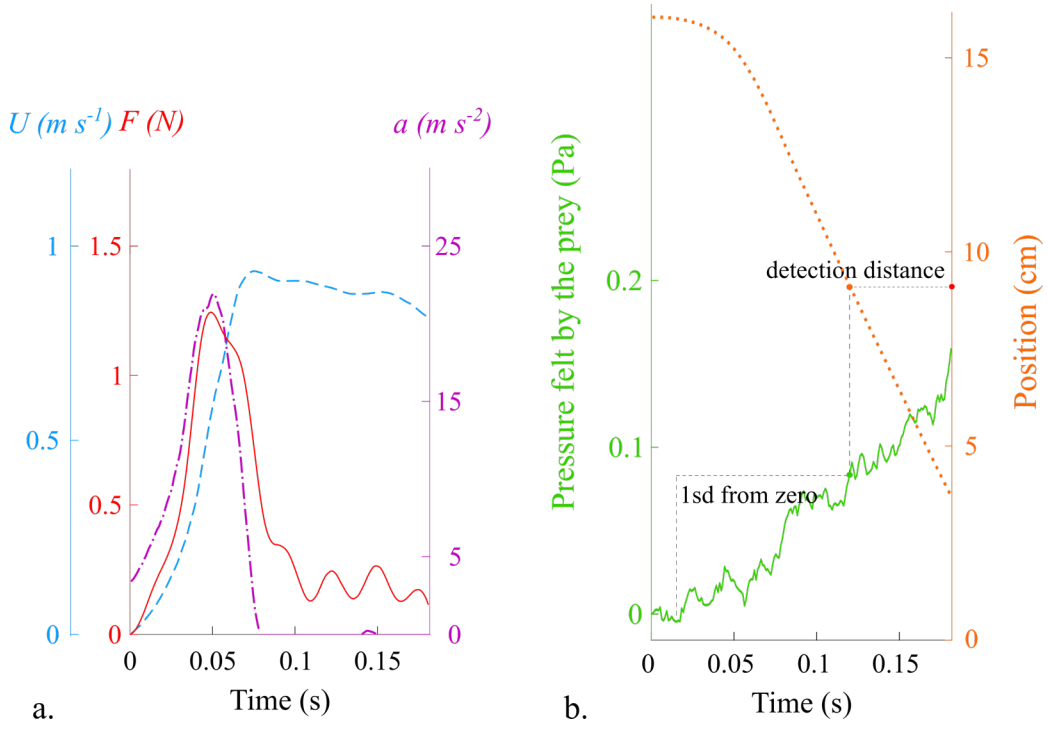

Figure 2: Example of the data obtained from one strike. a. Velocity (U; blue, dashed line) acceleration (a; purple, dashed and dotted line) and force applied on the model (F, sensor 1, Fig 1b.) according to time (s). Between 0-0.05 sec, the springs relax, therefore velocity, acceleration and force increase. After approximately 0.05 sec, the springs are fully extended and the acceleration decreases. When the acceleration is null, the velocity reaches its maximum (U_{max}) and the force recorded by the sensor corresponds to the steady drag ($F = F_d$, Eq (3)). b. Pressure recorded by the 'prey sensor' (sensor 2, Fig 1b.) and position of the model (orange, dotted line) according to time (s). When the model gets closer to the prey sensor, the pressure increases. Once the pressure deviates of 1 standard deviation from 0, we consider the prey triggered by the attack and defined the corresponding distance as the detection distance.

Particle Image Velocimetry

We used 2D Particle Image Velocimetry (PIV) with a high-speed camera, Dantec Dynamics SpeedSense M, to obtain a time-resolved recording of the strike from the bottom of

the tank (Fig. 1b.). Water was seeded with polyamid particles of 20 µm in diameter and a Quantronix® Darwin-Duo laser was used to produce the light sheet. Image acquisition was performed at 733 Hz. We choose to record three different planes on each head to obtain a complete picture of the fluid flow around the head during the attack (see Supplementary Material 3). These planes were obtained by rotating the model around the aluminum rod. We applied the same compression to the springs (i.e. maximal compression) to get an equivalent comparison for the different shapes. Acquisition was performed using the Dantec DynamicStudio 2015a software. The PIV vector computation was performed using LaVision 7.2 with a 16 x 16 pixel interrogation window and 50% overlap. Additional post-processing and analysis was done in Matlab using the PIVMat toolbox [38]. The flow features can be characterized by examining the vortex structures formed at the corner of the mouth and on both tips of the jaw and of the skull. We created videos of the vortex formation during a strike, obtained from PIV in three planes (see Materials and Methods section) to compare both models (see Supplementary videos SM4-5-6). A more quantitative analysis was performed by computing the overall primary circulation $\Gamma = \int \omega^{+} dA$ in each PIV plane (ω^{+} being the positive vorticity in Fig. 6b.). The evolution of the dimensionless circulation Γ/UL as a function of time, where L is the characteristic length scale of the acceleration regime of the strike maneuver (which is constant for all experiments) and U is the velocity of the strike is plotted in Fig. 6b.

Statistical analyses

To compare the detection distance, we ran an ANCOVA with the distance as the response variable, the model as a factor, and the acceleration as covariate as a snake strike is an accelerated motion. All the variables were Log_{10}-transformed and the statistical analyses were performed using R [39]. The significance level was set at 5%.

Results

Drag and added mass

The range of kinematics of our experiments fits the range of velocity and acceleration observed in live snakes during frontal strikes (U_{max}: live snakes: 0.24 – 1.7 m s^{-1}, experiments: 0.22 – 1.5 m s^{-1}; a_{max}: live snakes: 8.3 – 75 m s^{-2}, experiments: 3.4 – 40.4 m s^{-2})[14,16,40,41]. The duration of the acceleration (0.05 – 0.1 s) also fits in the range of duration of a real snake strike[42].

For each model, the instantaneous drag $F_{d(t)}$ has a smaller contribution to the peak force (i.e. during the acceleration phase) than the acceleration reaction F_a (Fig. 3.). The acceleration reaction is the predominant force for the aquatic model whereas, for the non-aquatic model, the steady drag is dominant. Force values between models are not directly comparable in Figure 3. as the specific characteristics of the models (e.g. frontal surface, volume…) are not considered. Only the drag and added mass coefficient allow to compare the impact of the shape on the forces.

The drag coefficient of the non-aquatic shape is larger than the coefficient of the aquatic model, respectively 0.58 and 0.24 (Fig. 4.). The mean added mass for the aquatic model is 12.67 g, which represents 26.9% of the mass of the model versus 15.48 g for the non-aquatic model which represent 37.7% for the mass of the model. The added mass coefficients obtained from the linear regression on Fig. 4. are 0.15 for the aquatic model and 0.24 for the non-aquatic model.

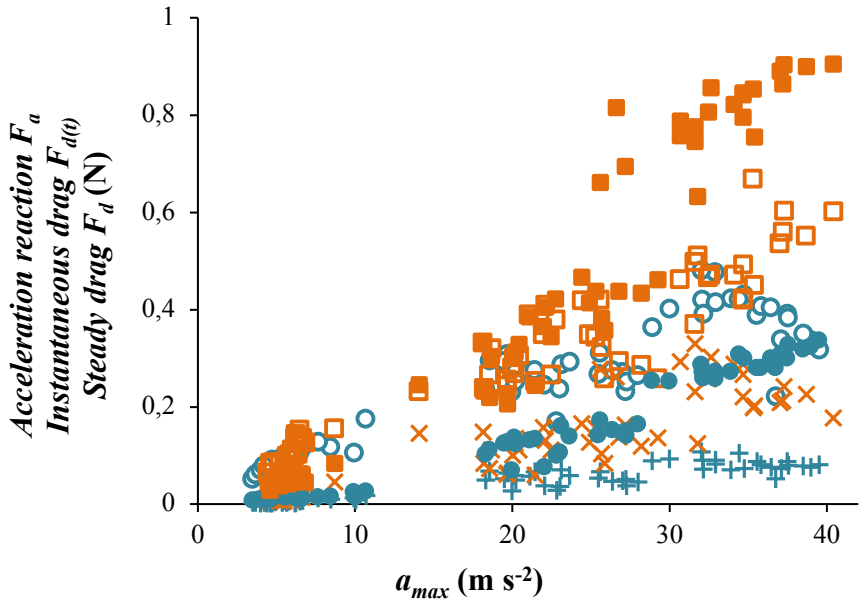

Figure 3: Respective contribution of the acceleration reaction (F_a; empty signs), the instantaneous drag during the peak force ($F_{d(t)}$; cross symbols for the non-aquatic, plus symbol for the aquatic model) and the steady drag (F_d; filled signs) according to the maximal acceleration (a_{max}) for each strike, for the non-aquatic (squares) and aquatic (circles) models.

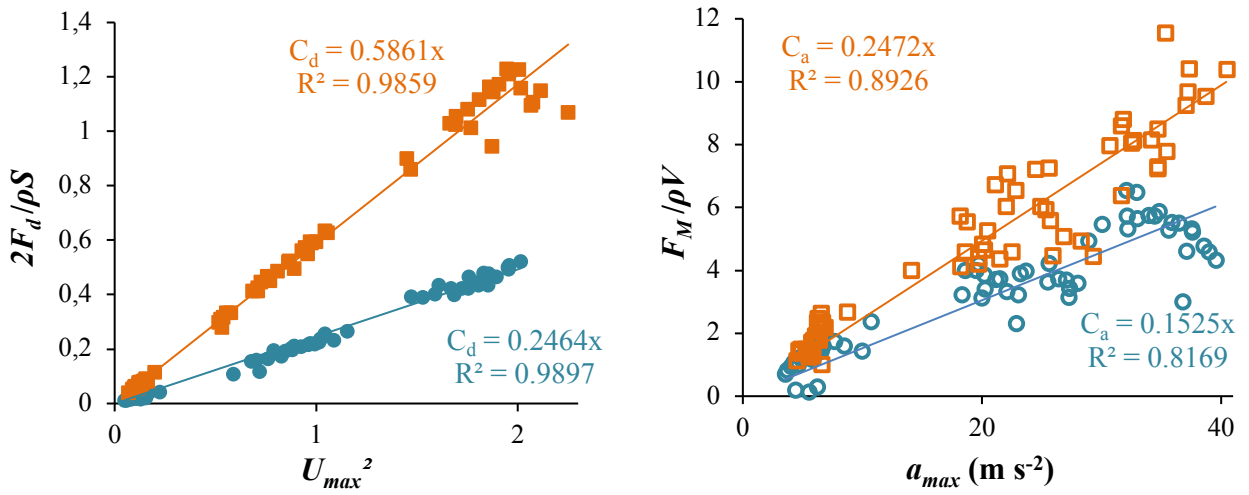

a. b.

Figure 4: Comparison of the hydrodynamic forces that apply on each model (squares: non-aquatic; circles: aquatic) depending on the kinematics of each strike (one point represents one strike) a. Representation of the steady drag (drag term $2F_d/\rho S$ of Eq (5)) depending on the squared velocity (U_{max}^2). b. Representation of the added mass force ($F_M/\rho V$ of Eq (7)) depending on the maximal acceleration (a_{max} in m s^{-2}). Linear regression lines are drawn. The slopes correspond to the drag and added mass coefficient, respectively C_d and C_a, of each shape and the R^2 are the regression coefficients.

Detection distance

The force signal was too noisy to obtain accurate measures of the detection distance at low velocities (i.e. U > 0.5 m s^{-1}). At higher speeds there is no statistical difference between the distances at which the prey could detect the presence of the snake depending on their head shape. However, this distance depends on the maximal acceleration of the strike, the higher the acceleration, the earlier the detection of the predator (ANCOVA: $F_{2,83} = 4.08$; $P = 0.02$; model: $P = 0.77$; a_{max}: $P = 0.001$) (Fig. 5.).

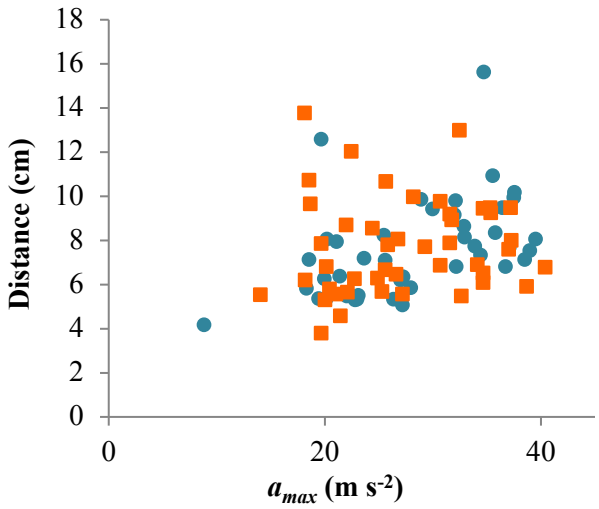

Figure 5: Distance (cm) at which the prey could potentially detect the snake depending on the maximal acceleration (m s^{-2}). For each graph: squares: non-aquatic model, circles: aquatic model. Each point represents a strike.

Flow characterization

The PIV measurements illustrate that the vortices are formed very early during the strike (see Supplementary videos SM4-5-6). For both models, the frontal strike maneuver involves strong flow separation due to the high shear produced by the impulsive acceleration. On the lateral side of the head (bottom view, Fig. 6a.), the number of vortices and the area they occupy and is smaller in the aquatic model, yet, the intensity of the vorticity is higher. The primary circulation in this area is slightly (~10%) lower over the whole acceleration phase for the aquatic model (Fig. 6b.). Below the jaw (jaw view, Fig. 6a.), the area occupied by the vortices is similar, yet the intensity of the vorticity is lower for the aquatic model. A much lower overall circulation is produced by the vorticity detached from the tip of the jaw in the aquatic case (around 40% of the non-aquatic value at the end of the acceleration phase). Behind the tip of the snout (skull view, Fig. 6a.), the area occupied by the vortices is larger and the vorticity is more intense for the aquatic model. The aquatic shape generates more overall circulation around the top of the head. Overall, the aquatic model seems to present smaller vortices, with slightly less overall circulation but more intense vorticity compared to the non-aquatic model.

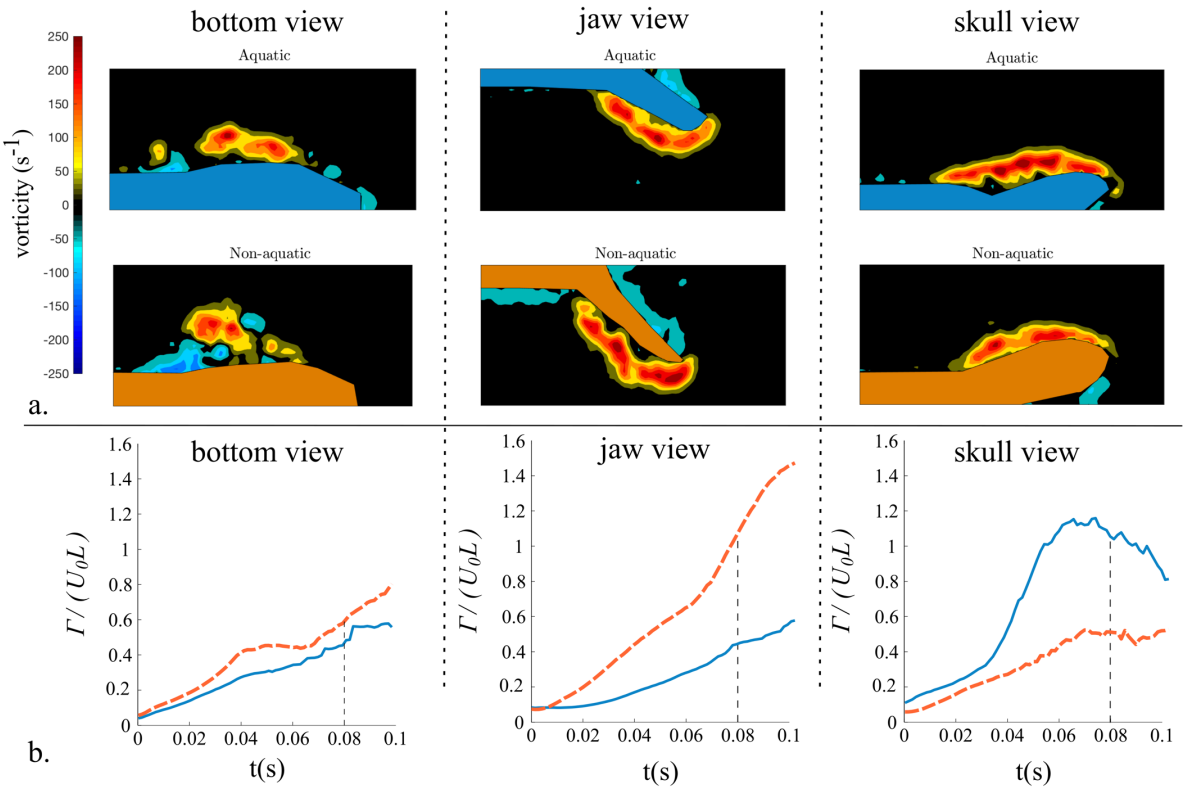

Figure 6: a. Snapshots of the vorticity field ω_z around the snake head models at the end of the acceleration phase (t ≈ 0.08 s) for the aquatic (first line) and non-aquatic (second line) models, in the three measurement planes: bottom, jaw and skull views are shown on the first to third columns, respectively. The color bar for the vorticity field is given in s^{-1}. b. Evolution of the dimensionless integrated positive circulation during the acceleration phase depending on the time for both models (dashed line for the non-aquatic model) in each of the three views considered. The end of the acceleration (t ≈ 0.08 s) is indicated on each graph.

Discussion

The aim of this study was to characterize and measure the hydrodynamic forces involved when a snake captures a prey under water using a frontal strike, and to evaluate how head shape might affect these forces. It should first be noticed that the kinematic profile of our experiment lies within the biological range of real snake strikes. Second, we validated our hypothesis of a significant hydrodynamic advantage of the convergent head shape observed in aquatic snakes. However, we did find that shape differentially affects the steady drag and the acceleration reaction. Drag is well known for its importance during steady locomotion but it is also involved

in transient behaviors such as the capture maneuver studied here. Certainly, the aquatic shape appears better adapted to capture aquatic prey using a frontal strike than the non-aquatic shape, at least in terms of drag. The aquatic model has a drag coefficient that is more than two times smaller than the non-aquatic model. The drag coefficient of the aquatic model is consistent with previous fluid dynamic simulation of a prey capture in an aquatic snake, *Natrix tessellata*, at 1 m s^{-1} with a gape angle of 70° (C_d= 0.25)[28]. The contribution of the instantaneous drag represents 2.7% of the peak of force for the aquatic shape whereas it is 7.6% for the non-aquatic model. Additionally, figure 3 suggests that drag seems to play a larger role in the hydrodynamics of the non-aquatic model as it is, quantitatively, the larger force for this model. The contribution of acceleration reaction is slightly larger than the steady drag for the aquatic model. As for crayfish[38], drag does not seem to be the major hydrodynamic constraint to overcome during a transient maneuver. During crayfish escape response, 90% of the resistive force comes from the mass and added mass. In our experiment, inertia-related forces represent 92.4% of the strike for the non-aquatic model and 97.3% of the aquatic model. However, when the forces are rendered non-dimensional (Fig. 4), the aquatic model has a more hydrodynamic profile, with a smaller drag coefficient and a smaller added mass. Unlike the body of fish[26], the head shape of a snake appears not to generate a morphological trade-off between drag and added mass. To place our results in a broader context, the drag coefficient of a sphere and a circular cylinder, at the same Reynolds number as our experiment, are respectively 0.47 and 1. Their added mass coefficient value is close to their drag coefficient (C_{a_sphere} = 0.5; $C_{a\_cylinder}$ = 1)[2]. Regarding the drag, our aquatic model is better streamlined than a sphere, but the non-aquatic model is positioned between the sphere and a circular cylinder. Whereas, for the added mass coefficient of our two models are below those of both simple geometries.

Looking at the flow pattern around the head models (Fig. 6), the hydrodynamic advantage of the aquatic snake could potentially be related to a smaller primary vortex on the side of the head, the non-aquatic snake showing a more fluctuating and disordered flow field. Moreover, the vorticity produced at the tip of the jaw shows a clear quantitative difference and is consistently higher for the non-aquatic model. However, the skull view shows the opposite pattern of vorticity; the non-aquatic shape produces fewer vortices with an integrated primary circulation that is less important than for the aquatic model. It should be noted that the 2D nature of the PIV measurements presented here does not allow us to provide a quantitative link between

the vorticity profile of the flow around the head and the hydrodynamic forces. Nonetheless, from the present results we can conjecture that a reduction of the recirculation bubble behind the jaw may be one of the main physical mechanisms explaining the physical advantage of the head shape observed in aquatically foraging snakes.

Regarding the prey detection distance, our results show that this distance does not depend on the snake head shape, but rather that it increases with strike velocity. However, we cannot conclude on the biological relevance of the absolute prey detection distance measured in our experiment as our setup was built with as primary purpose to measure drag and added mass. Snakes usually strike when the prey is close to their head (e.g. 0.5-0.8 cm for *Erpeton tentaculatum* [41]; 4.87 cm for *T. couchii*; 2.81 cm for *T rufipunctatus* [12]; less than 3 cm for *Hydrophis schistosus* [43]). The detection distance measured here is around 6 to 10 cm, so we could consider that the prey can possibly detect the snake almost instantaneously upon the strike initiation, the reaction time of a fish being around 7 ms [41]. Capture success is thus more likely determined by the hydrodynamic profile of the snake head than being dependent on the reaction of the prey. Moreover, some snakes are known to purposefully trigger the fast escape response of the prey in order to catch them[41].

In conclusion, we investigated the role of head shape on the hydrodynamic forces generated by a predator using an experimental approach focusing on a transient maneuver. We were able to quantify the role and impact of head shape on the hydrodynamics of prey capture in aquatic snakes. We highlighted a clear hydrodynamic advantage of the aquatic head shape when capturing a prey being associated not only with a smaller drag coefficient but also a smaller added mass coefficient. These results validate the hypothesis that the morphological convergence of the head shape in aquatic snakes is an adaptation to an aquatic lifestyle as it provides a clear hydrodynamic advantage. In this work, we focused on the shape of the head of aquatically foraging snakes, as several studies have highlighted convergence therein, and as shape is directly related to hydrodynamic constraints. Size could be another important feature regarding the hydrodynamic constraints. However, we did not detect any allometry in our morphological study, meaning that the aquatically foraging snakes are not significantly different in size than their closely related non-aquatic species. Thus, the present work focuses on the functional meaning of shape irrespective of size. The other factors that could play a role in the

hydrodynamics of the prey capture of aquatic snakes could be the gape angle and macro and microscopic skin features which remains to be investigated. The versatility of snake locomotion has raised the attention of engineers and spurred the development of snake-inspired robots that can move both on land and in water[42] . However, whereas most biomechanical studies have focused the role of the body during steady locomotion, our results show that the head shape is crucial in transient maneuvers and should thus be considered when designing underwater vehicles or robots needing to perform fast transient maneuvers.

391 **References**

392 1. Webb, P. W. Simple physical principles and vertebrate aquatic locomotion. *Integr.*
393 *Comp. Biol.* **28,** 709–725 (1988).

394 2. Vogel, S. *Life In Moving Fluids: The Physical Biology Of Flow*. (Princeton University
395 Press, 1994).

396 3. Hoerner, S. F. *Fluid Dynamic Drag*. (Hoerner Fluid Dynamics, 1965).

397 4. Godoy-Diana, R. & Thiria, B. On the diverse roles of fluid dynamic drag in animal
398 swimming and flying. *J. R. Soc. Interface* **15,** 20170715 (2018).

399 5. Daniel, T. L. Unsteady aspects of aquatic locomotion. *Am. Zool.* **24,** 121–134 (1984).

400 6. Brennen, C. E. A review of added mass and fluid inertial forces. (1982).

401 7. Bilcke, J., Herrel, A. & Aerts, P. Effect of prey and predator size on the capture success
402 of an aquatic snake. *Belgian J. Zool.* **137,** 191–195 (2007).

403 8. Kelley, N. P. & Motani, R. Trophic convergence drives morphological convergence in
404 marine tetrapods. *Biol. Lett.* **11,** 5 (2015).

405 9. Howell, A. B. *Aquatic Mammals*. (Dover Publications Inc, 1971).

406 10. Winemiller, K. O., Kelso-Winemiller, L. C. & Brenkert, A. L. Ecomorphological
407 diversification and convergence in fluvial cichlid fishes. *Environ. Biol. Fishes* **44,** 235–
408 261 (1995).

409 11. Taylor, M. A. How tetrapods feed in water: a functional analysis by paradigm. *Zool. J.*
410 *Linn. Soc.* **91,** 171–195 (1987).

411 12. Alfaro, M. E. Forward attack modes of aquatic feeding garter snakes. *Funct. Ecol.* **16,**
412 204–215 (2002).

413 13. Alfaro, M. E. Sweeping and striking: a kinematic study of the trunk during prey capture
414 in three thamnophiine snakes. *J. Exp. Biol.* **206,** 2381–2392 (2003).

14. Bilcke, J., Herrel, A. & Van Damme, R. Correlated evolution of aquatic prey-capture strategies in European and American natricine snakes. *Biol. J. Linn. Soc.* **88,** 73–83 (2006).

15. Herrel, A. *et al.* Morphological convergence as a consequence of extreme functional demands: examples from the feeding system of natricine snakes. *J. Evol. Biol.* **21,** 1438–1448 (2008).

16. Vincent, S. E., Herrel, A. & Irschick, D. J. Comparisons of aquatic versus terrestrial predatory strikes in the pitviper, Agkistrodon piscivorus. *J. Exp. Zool. Part A Comp. Exp. Biol.* **303,** 476–488 (2005).

17. Drummond, H. M. Aquatic Foraging in Garter Snakes : A Comparison of Specialists and Generalists. *Behavior* **86,** 1–30 (1983).

18. Lauder, G. V. & Prendergast, T. Kinematics of aquatic prey capture in the snapping turtle Chelydra serpentina. *J. Exp. Biol.* **164,** 55–78 (1992).

19. Summers, A. P., Darouian, K. F., Richmond, A. M. & Brainerd, E. L. Kinematics of Aquatic and Terrestrial Prey Capture in Terrapene carolina, With Implications for the Evolution of Feeding in Cryptodire Turtles. *J. Exp. Zool.* **281,** 280–287 (1998).

20. Van Damme, J. & Aerts, P. Kinematics and functional morphology of aquatic feeding in Australian snake-necked turtles (Pleurodira;Chelodina). *J. Morphol.* **233,** 113–25 (1997).

21. Langebartel, D. A. in *Illinois biological monographs, 38* 180 (Urbana, University of Illinois Press, 1968).

22. Vincent, S. E., Brandley, M. C., Herrel, A. & Alfaro, M. E. Convergence in trophic morphology and feeding performance among piscivorous natricine snakes. *J. Evol. Biol.* **22,** 1203–1211 (2009).

23. Esquerré, D. & Keogh, J. S. Parallel selective pressures drive convergent diversification of phenotypes in pythons and boas. *Ecol. Lett.* **19,** 800–809 (2016).

441 24. Hibbitts, T. J. & Fitzgerald, L. A. Morphological and ecological convergence in two
442 natricine snakes. *Biol. J. Linn. Soc.* **85,** 363–371 (2005).

443 25. Segall, M., Cornette, R., Fabre, A.-C., Godoy-Diana, R. & Herrel, A. Does aquatic
444 foraging impact head shape evolution in snakes ? *Proc. R. Soc. London, B Biol. Sci.*
445 **283,** (2016).

446 26. Webb, P. W. Body form, locomotion and foraging in aquatic vertebrates. *Am. Zool.* **24,**
447 107–120 (1984).

448 27. Young, B. A. The influences of the aquatic medium on the prey capture system of
449 snakes. *J. Nat. Hist.* **25,** 519–531 (1991).

450 28. Van Wassenbergh, S. *et al.* Hydrodynamic constraints on prey-capture performance in
451 forward-striking snakes. *J. R. Soc. Interface* **7,** 773–785 (2010).

452 29. van Netten, S. M. Hydrodynamic detection by cupulae in a lateral line canal: functional
453 relations between physics and physiology. *Biol. Cybern.* **94,** 67–85 (2006).

454 30. McHenry, M. J., Feitl, K. E., Strother, J. A. & Van Trump, W. J. Larval zebrafish
455 rapidly sense the water flow of a predator's strike. *Biol. Lett.* **5,** 477–9 (2009).

456 31. Thiria, B., Goujon-Durand, S. & Wesfreid, J. E. The wake of a cylinder performing
457 rotary oscillations. *J. Fluid Mech.* **560,** 123–147 (2006).

458 32. Saffman, P. G. *Vortex Dynamics*. (Cambridge University Press, 1992).

459 33. Ringuette, M. J., Milano, M. & Gharib, M. Role of the tip vortex in the force generation
460 of low-aspect-ratio normal flat plates. *J. Fluid Mech.* **581,** 453 (2007).

461 34. Dryden, I. L. & Mardia, K. V. *Statistical Shape Analysis with Apllications in R, Second*
462 *Edition*. (Wiley, 2016).

463 35. Penning, D. A., Sawvel, B. & Moon, B. R. Debunking the viper's strike: Harmless
464 snakes kill a common assumption. *Biol. Lett.* **12,** 1–4 (2016).

465 36. Radford, C. A., Montgomery, J. C., Caiger, P. & Higgs, D. M. Pressure and particle

motion detection thresholds in fish: a re-examination of salient auditory cues in teleosts. *J. Exp. Biol.* **215,** 3429–3435 (2012).

37. Kastelein, R. A. *et al.* Startle response of captive North Sea fish species to underwater tones between 0.1 and 64 kHz. *Mar. Environ. Res.* **65,** 369–377 (2008).

38. Moisy, F. A PIV Post-processing and data analysis toolbox : PIVMat 4.00 27 Apr 2006 (Updated 26 Apr 2016). (2006).

39. R Development Core Team. *R: A language and environment for statistical computing.* (2014).

40. Smith, T. L., Povel, G. D. E., Kardong, K. V., Povel, D. E. & Kardong, K. V. Predatory strike of the tentacled snake (Erpeton tentaculatum). *J. Zool. London* **256,** 233–242 (2002).

41. Catania, K. C. Tentacled snakes turn C-starts to their advantage and predict future prey behavior. *Proc. Natl. Acad. Sci. U. S. A.* **106,** 11183–7 (2009).

42. Lillywhite, H. B. *How snakes work: structure, function and behavior of the World's snakes*. (Oxford University Press, 2014).

43. Voris, H. K., Voris, H. H. & Liat, L. B. The food and feeding behavior of a marine snake, Enhydrina schistosa (Hydrophiidae). *Copeia* **1978,** 134–146 (1978).

Videos of frontal strikes in snakes:

https://www.youtube.com/watch?v=6sC6iiCWyw4

https://www.youtube.com/watch?v=4_v5THJuorw&t=53s

https://www.youtube.com/watch?v=sPszRWCgJ-A

Acknowledgments

We thank Olivier Brouard, Amaury Fourgeaud and Tahar Amorri from the PMMH lab for their precious help in the experimental design as well as Xavier Benoit-Gonin for his help with the 3D printer. Thierry Darnige and especially Justine Laurent are acknowledged for their

help with the sensors and computer coding. MS acknowledge the different referees and Dr Izzet for their contribution to improve this manuscript. MS thanks the Région Ile de France for funding this research project and the doctoral school Frontières du Vivant (FdV) – Programme Bettencourt.

Author contributions

All authors helped revise and approved the manuscript and conceived the study. MS carried out the data collection, the statistical analyses, and wrote the manuscript. RGD helped to build the experimental setup and to interpret the data. RGD carried out the particle image velocimetry analysis. AH participated in the scientific interpretation of the data in a biological context.

Competing interests

We have no competing interests.

Data availability

See Supplementary Table S5

Figure and table legends

Figure 1: a. 3D models of the head shape of aquatic (first line) and non-aquatic snakes (second line) in front, side and top view (see also Supplementary Material 1). b. Experimental setup used to mimic the frontal attack of a snake towards a prey (see also Supplementary Material 2). The snake model is directly linked to the force sensor 1 which is itself vertically attached to the mobile part of the air-bearing rail. The force sensor 2 is placed at the end of the track. It is recording the pressure variation thanks to a round plate attached to the sensor (vertical grey line). The directions of the positive forces of each sensor is indicated ($F > 0$). The position sensor is placed at the end of the track, on the rail. The horizontal green line represents the PIV laser sheet. The model is turned to obtain three different views of the flow pattern around the head (see Supplementary Material 3).

Figure 2: Example of the data obtained from one strike. a. Velocity (U; blue, dashed line) acceleration (a; purple, dashed and dotted line) and force applied on the model (F, sensor 1, Fig 1b.) according to time (s). Between 0-0.05 sec, the springs relax, therefore velocity, acceleration

and force increase. After approximately 0.05 sec, the springs are fully extended and the acceleration decreases. When the acceleration is null, the velocity reaches its maximum (U_{max}) and the force recorded by the sensor corresponds to the steady drag ($F = F_d$, Eq (3)). b. Pressure recorded by the 'prey sensor' (sensor 2, Fig 1b.) and position of the model (orange, dotted line) according to time (s). When the model gets closer to the prey sensor, the pressure increases. Once the pressure deviates of 1 standard deviation from 0, we consider the prey triggered by the attack and defined the corresponding distance as the detection distance.

Figure 3: Respective contribution of the acceleration reaction (F_a; empty signs), the instantaneous drag during the peak force ($F_{d(t)}$; cross symbols for the non-aquatic, plus symbol for the aquatic model) and the steady drag (F_d; filled signs) according to the maximal acceleration (a_{max}) for each strike, for the non-aquatic (squares) and aquatic (circles) models.

Figure 4: Comparison of the hydrodynamic forces that apply on each model (squares: non-aquatic; circles: aquatic) depending on the kinematics of each strike (one point represents one strike) a. Representation of the steady drag (drag term $2F_d/\rho S$ of Eq (5)) depending on the squared velocity (U_{max}^2). b. Representation of the added mass force ($F_M/\rho V$ of Eq (7)) depending on the maximal acceleration (a_{max} in m s^{-2}). Linear regression lines are drawn. The slopes correspond to the drag and added mass coefficient, respectively C_d and C_a, of each shape and the R^2 are the regression coefficients.

Figure 5: Distance (cm) at which the prey could potentially detect the snake depending on the maximal acceleration (m s^{-2}). For each graph: squares: non-aquatic model, circles: aquatic model. Each point represents a strike.

Figure 6: a. Snapshots of the vorticity field ω_z around the snake head models at the end of the acceleration phase ($t \approx 0.08$ s) for the aquatic (first line) and non-aquatic (second line) models, in the three measurement planes: bottom, jaw and skull views are shown on the first to third columns, respectively. The color bar for the vorticity field is given in s^{-1}. b. Evolution of the dimensionless integrated positive circulation during the acceleration phase depending on the time for both models (dashed line for the non-aquatic model) in each of the three views considered. The end of the acceleration ($t \approx 0.08$ s) is indicated on each graph.

Table 1: Characteristics of each model.